Rapid Communications

ωN scattering length from ω photoproduction on the proton near the reaction threshold

T. Ishikawa,[1,*] H. Fujimura,[1,†] H. Fukasawa,[1] R. Hashimoto,[1,‡] Q. He,[1,§] Y. Honda,[1] A. Hosaka,[2,3] T. Iwata,[4] S. Kaida,[1] J. Kasagi,[1] A. Kawano,[5] S. Kuwasaki,[1] K. Maeda,[6] S. Masumoto,[7] M. Miyabe,[1] F. Miyahara,[1,‖] K. Mochizuki,[1] N. Muramatsu,[1] A. Nakamura,[1] S. X. Nakamura,[8] K. Nawa,[1] S. Ogushi,[1] Y. Okada,[1] K. Okamura,[1] Y. Onodera,[1] K. Ozawa,[9] Y. Sakamoto,[5] M. Sato,[1] T. Sato,[2] H. Shimizu,[1] H. Sugai,[1,¶] K. Suzuki,[1,**] Y. Tajima,[4] S. Takahashi,[1] Y. Taniguchi,[1] Y. Tsuchikawa,[1,††] H. Yamazaki,[1,‡‡] R. Yamazaki,[1] and H. Y. Yoshida[4]

[1]*Research Center for Electron Photon Science (ELPH), Tohoku University, Sendai, Miyagi 982-0826, Japan*
[2]*Research Center for Nuclear Physics (RCNP), Osaka University, Ibaraki 567-0047, Japan*
[3]*Advanced Science Research Center, Japan Atomic Energy Agency (JAEA), Tokai 319-1195, Japan*
[4]*Department of Physics, Yamagata University, Yamagata 990-8560, Japan*
[5]*Department of Information Science, Tohoku Gakuin University, Sendai 981-3193, Japan*
[6]*Department of Physics, Tohoku University, Sendai 980-8578, Japan*
[7]*Department of Physics, University of Tokyo, Tokyo 113-0033, Japan*
[8]*Department of Modern Physics, University of Science and Technology of China, Hefei 230026, China*
[9]*Institute of Particle and Nuclear Studies, High Energy Accelerator Research Organization (KEK), Tsukuba 305-0801, Japan*

(Received 8 April 2019; revised manuscript received 16 February 2020; accepted 14 April 2020; published 6 May 2020)

Photoproduction of the ω meson on the proton has been experimentally studied near the threshold. The total cross sections are determined at incident energies ranging from 1.09 to 1.15 GeV. The 1/2 and 3/2 spin-averaged scattering length $a_{\omega p}$ and effective range $r_{\omega p}$ between the ω meson and proton are estimated from the shape of the total cross section as a function of the incident photon energy: $a_{\omega p} = (-0.97^{+0.16_{\rm stat}+0.03_{\rm syst}}_{-0.16_{\rm stat}-0.00_{\rm syst}}) + i(0.07^{+0.15_{\rm stat}+0.17_{\rm syst}}_{-0.14_{\rm stat}-0.09_{\rm syst}})$ fm and $r_{\omega p} = (+2.78^{+0.67_{\rm stat}+0.11_{\rm syst}}_{-0.54_{\rm stat}-0.12_{\rm syst}}) + i(-0.01^{+0.46_{\rm stat}+0.06_{\rm syst}}_{-0.50_{\rm stat}-0.00_{\rm syst}})$ fm, resulting in a repulsive force. The real and imaginary parts for $a_{\omega p}$ and $r_{\omega p}$ are determined separately for the first time. A small P-wave contribution does not affect the obtained values.

DOI: 10.1103/PhysRevC.101.052201

The structure of hadrons and dynamical hadron-mass generation are the most important subjects to be studied in the nonperturbative domain of quantum chromodynamics (QCD). The ω meson (ω) is one of the best established hadrons and is considered to give a short-ranged repulsive central force and a strong spin-orbit force between two nucleons (Ns) [1]. Nevertheless, the fundamental properties of ω such as the interaction with N is not known yet due to the difficulties in realizing scattering experiments. Detailed information on ωN scattering would not only reveal highly excited nucleon resonances (N^*) but also have a strong relevance to the equation of state (EoS) describing the interior of neutron stars [2]. Gravitational wave observations just have begun to provide information on the EoS [3].

The low-energy ωN scattering is characterized by the scattering length $a_{\omega N}$ and effective range $r_{\omega N}$ through an effective-range expansion of the S-wave phase shift $\delta(p)$:

$$p\cot\delta(p) = \frac{1}{a_{\omega N}} + \frac{1}{2}r_{\omega N}p^2 + O(p^4), \tag{1}$$

where p denotes the momentum of ω in the ωN center-of-mass (c.m.) frame. A positive (negative) Re $a_{\omega N}$ gives attraction (repulsion), and a positive Im $a_{\omega N}$ corresponds to the absorption to another channel such as $\omega N \to \pi N$. The $r_{\omega N}$ provides the momentum dependence of the interaction. Recently, the A2 collaboration at the Mainz MAMI facility has reported $|a_{\omega N}| = 0.82 \pm 0.03$ fm, which is extracted from ω photoproduction on the proton ($\gamma p \to \omega p$) near the threshold assuming a vector-meson dominance (VMD) model [4]. The obtained value is a combination of two independent S-wave scattering

*ishikawa@lns.tohoku.ac.jp
†Present address: Department of Physics, Wakayama Medical University, Wakayama 641-8509, Japan.
‡Present address: Institute of Materials Structure Science (IMSS), KEK, Tsukuba 305-0801, Japan.
§Present address: Department of Nuclear Science and Engineering, Nanjing University of Aeronautics and Astronautics (NUAA), Nanjing 210016, China.
‖Present address: Accelerator Laboratory, KEK, Tsukuba 305-0801, Japan.
¶Present address: Gunma University Initiative for Advanced Research (GIAR), Maebashi 371-8511, Japan.
**Present address: The Wakasa Wan Energy Research Center, Tsuruga 914-0192, Japan.
††Present address: Department of Physics, Nagoya University, Nagoya 464-8602, Japan.
‡‡Present address: Radiation Science Center, KEK, Tokai 319-1195, Japan.

lengths with total spins of 1/2 and 3/2. The unknown sign of $a_{\omega N}$ leaves the naive question of whether low-energy ωN scattering is repulsive or attractive.

Theoretically estimated values of $a_{\omega N}$ are scattered over a wide range from attractive to repulsive ones. The effective Lagrangian approach based on chiral symmetry gives an attractive value of $a_{\omega N} = +1.6 + i0.30$ fm [5]. A QCD sum-rule analysis provides a weakly attractive value of $a_{\omega N} = +0.41 \pm 0.05$ fm [6]. The coupled-channel unitary approach gives repulsive values of $a_{\omega N}^{(1/2)} = -0.45 + i0.31$ fm and $a_{\omega N}^{(3/2)} = -0.43 + i0.15$ fm for the two total spins, giving a spin-averaged value of $a_{\omega N} = -0.44 + i0.20$ fm [7]. The coupled-channel analysis of ω production in pion and photoinduced reactions gives a very weakly repulsive value of $a_{\omega N} = -0.026 + i0.28$ fm [8]. The dynamical coupled-channel analysis resulted in $a_{\omega N}^{(1/2)} = 0.0454 + i0.0695$ fm and $a_{\omega N}^{(3/2)} = -0.180 + i0.0597$ fm, giving a repulsive spin-averaged value[1] of $a_{\omega N} = -0.135 + i0.0630$ fm [9]. Neither the coupled-channel analyses nor the VMD analysis by the A2 collaboration incorporates the finite width of ω in the final state.

To determine the low-energy ωN scattering parameters $a_{\omega N}$ and $r_{\omega N}$ experimentally, we investigate the $\gamma p \to \omega p$ reaction very close to the reaction threshold. Several collaborations have already measured the total cross sections near the threshold by using the $\omega \to \pi^+\pi^-\pi^0$ decay mode (SAPHIR [10] and CLAS [11] Collaborations), and the $\omega \to \pi^0\gamma$ decay mode (CBELSA-TAPS [12] and A2 [4] Collaborations). Currently, the data points for the total cross section near the threshold ($E_\gamma \lesssim 1.2$ GeV), where the S-wave ωN contribution is dominant, are not enough for determining $a_{\omega N}$ and $r_{\omega N}$ from the shape of the total cross section as a function of the incident energy (excitation function) through ωN rescattering in the final-state interaction. We have measured ten data points of the total cross section at incident photon energies ranging from 1.09 to 1.15 GeV. The ω meson mainly decays in the $\omega \to \pi^0\pi^+\pi^-$ mode with a branching ratio of 89.2% [13]. It is, however, difficult to reproduce the background shapes in the $\pi^0\pi^+\pi^-$ invariant-mass distributions measured with poor identification for charged particles [14]. Thus, we determined the cross sections using the $\omega \to \pi^0\gamma$ decay mode with a branching ratio of 8.40%. In this Rapid Communication, we present $a_{\omega N}$ and $r_{\omega N}$ extracted from the shape of the excitation function for the $\gamma p \to \omega p$ reaction.

A series of meson photoproduction experiments were conducted [15] using the FOREST detector [16], which was installed on the second photon beamline [17] at the Research Center for Electron Photon Science (ELPH), Tohoku University, Japan. In the present experiments, bremsstrahlung photons were produced from 1.2 GeV circulating electrons in a synchrotron [18] by inserting a carbon thread (radiator) [17]. The photons collimated with two lead apertures of 10 and 25 mm in diameter located 4.2 and 12.9 m downstream from the radiator, respectively, were incident on a 45-mm-thick liquid-hydrogen target located at the center of FOREST. The energies of the incident photons were analyzed up to 1.15 GeV by detecting the postbremsstrahlung electrons with a photon-tagging counter, STB-Tagger II [17]. FOREST consists of three different electromagnetic calorimeters (EMCs): 192 undoped CsI crystals, 252 lead scintillating-fiber modules, and 62 lead glasses. A plastic-scintillator hodoscope (PSH) is placed in front of each EMC to identify charged particles. FOREST covers a solid angle of ≈88% in total. The typical photon-tagging rate was 20 MHz, and the photon transmittance (the so-called tagging efficiency) was ≈53% [17]. The trigger condition of the data acquisition (DAQ), which required for an event to have more than one final-state particles in coincidence with a photon-tagging signal [16], was the same as that in Ref. [19]. The total number of collected events in DAQ was 1.79×10^9. The average trigger rate was 1.6 kHz, and the average DAQ efficiency was 80%.

Event selection was made for the $\gamma p \to \pi^0\gamma p \to \gamma\gamma\gamma p$ reaction. To find the corresponding events containing three neutral particles and a charged particle within a 14 ns time window, we scanned all the combinations for three neutral EMC clusters. We required the following conditions for each combination: (1) the time difference between every two neutral EMC clusters out of three was less than thrice that of the time resolution for the difference; (2) the $\gamma\gamma$ invariant mass for the two neutral EMC clusters ranged from 50 to 220 MeV; (3) the remained EMC cluster had an energy higher than 200 MeV; (4) the charged particles were detected with the forward PSH in the time delay within $[-2, 12)$ ns from the response of three neutral clusters; (5) no other particles were found in the same time window. No events provide more than one combination. Further selection was made by applying a kinematic fit with five constraints: energy and three-momentum conservation, and $\gamma\gamma$ invariant mass being the π^0 mass. The momentum of the charged particle was obtained from the time delay by assuming that the charged particle had proton mass. Events for which the χ^2 probability was higher than 0.1 were selected. When the number of combinations was more than one in an event, the combination with the minimum χ^2 was adopted. Sideband-background subtraction was performed for accidental-coincidence events detected in STB-Tagger II and FOREST.

All the data for incident energies above 1.09 GeV (E_γ = 1.09–1.15 GeV) are divided into ten bins (every bin includes four photon-tagging channels), and ten angular bins of the $\pi^0\gamma$ emission angle $\cos\theta$ in the γp-c.m. frame. The typical $\pi^0\gamma$ invariant-mass ($M_{\pi\gamma}$) distributions are shown in Fig. 1. Each $M_{\pi\gamma}$ distribution shows a prominent peak with a centroid of ≈0.78 GeV, and has a broad background contribution in the lower side. This background contribution is well reproduced by a Monte Carlo (MC) simulation based on GEANT4 [20] for the $\gamma p \to \pi^0\pi^0 p \to \gamma\gamma\gamma\gamma p$ reaction, where one γ out of four is not detected with FOREST. In the simulation, the fivefold differential cross sections are assumed to be the same as those provided by the 2-PIOIN-MAID calculation [21]. The $M_{\pi\gamma}$ distributions for the $\gamma p \to \pi^0\pi^0 p$ reaction are also plotted in Fig. 1 where the same analysis is applied as for the $\gamma p \to \pi^0\gamma p$ reaction.

[1]We adopt $a_{\omega N} = (1/3)a_{\omega N}^{(1/2)} + (2/3)a_{\omega N}^{(3/2)}$ for the spin average using the convention of Lutz *et al.* [7,8].

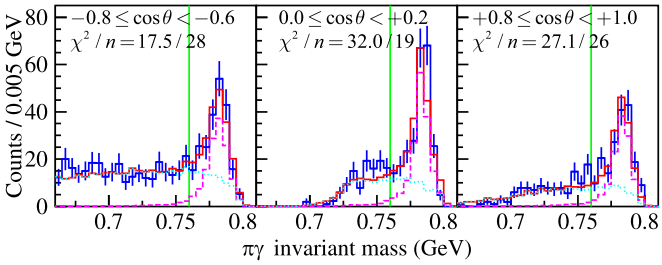

FIG. 1. Typical $M_{\pi\gamma}$ distributions for the highest incident energy group ($E_\gamma = 1.144$–1.149 GeV). In each panel, the histogram (blue) shows the experimentally obtained $M_{\pi\gamma}$ distribution, and the solid curve (red) shows the sum of the $M_{\pi\gamma}$ distributions obtained in the simulation for the $\gamma p \to \omega p \to \pi^0\gamma p$ and $\gamma p \to \pi^0\pi^0 p$ reactions. The dashed (magenta) and dotted (cyan) curves show these contributions. The angular region of ω emission in the γp-c.m. frame is described in each panel. The vertical lines show the lower limit $M_{\pi\gamma} = 0.76$ GeV for selecting the ω-produced events.

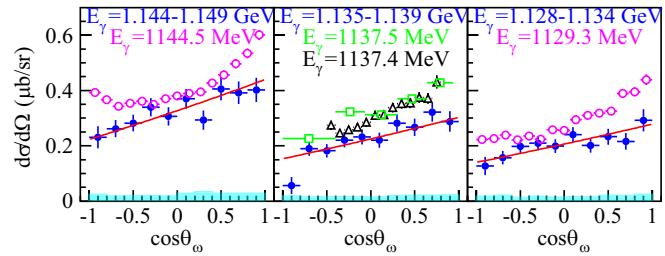

FIG. 2. Typical angular differential cross sections $d\sigma/d\Omega$ as a function of the ω emission angle $\cos\theta$ in the γp-c.m. frame. The range of the incident photon energies is described in each panel. The filled circles (blue) represent the measured $d\sigma/d\Omega$ in this work. The shaded areas represent the systematic uncertainties of $d\sigma/d\Omega$s. The solid curves show the fitted distribution with a P-wave contribution of $\sigma^P_{\max}/5$ (see text). The $d\sigma/d\Omega$ results from SAPHIR [10], CLAS [11], and A2 [4] collaborations are depicted by open boxes (green), open triangles (black), and open circles (magenta), respectively. The photon-energy coverages are 25, 18, 15, and ≈4.5 MeV in SAPHIR, CLAS, A2, and our results, respectively. The median of each coverage is described in the same color in the corresponding panel as data points.

The $M_{\pi\gamma}$ distributions for the $\gamma p \to \omega p \to \pi^0\gamma p \to \gamma\gamma\gamma p$ and $\gamma p \to \pi^0\pi^0 p \to \gamma\gamma\gamma\gamma p$ reactions in the MC simulation are fit to the measured $M_{\pi\gamma}$ distribution for each emission-angle and incident-energy bin only by changing the normalization coefficients. Here, the events are generated according to the pure phase space for the $\gamma p \to \omega p$ reaction. The number of the ω produced events N_ω is estimated for $M_{\pi\gamma} \geqslant 0.76$ GeV after subtracting the background $\gamma p \to \pi^0\pi^0 p$ contribution for each bin. The angular differential cross section is obtained from $N_\omega(\cos\theta)$ as

$$\frac{d\sigma}{d\Omega} = \frac{N_\omega(\cos\theta)}{2\pi\,\Delta\cos\theta N_\gamma N_\tau \eta_{\rm acc}(\cos\theta){\rm BR}(\omega \to \gamma\gamma\gamma)}, \quad (2)$$

with the incident photon flux including the DAQ efficiency correction N_γ, the number of target protons N_τ, the multiplication of branching ratios for the $\omega \to \pi^0\gamma$ and $\pi^0 \to \gamma\gamma$ decays ${\rm BR}(\omega \to \gamma\gamma\gamma)$, and the detector acceptance calculated in the simulation $\eta_{\rm acc}(\cos\theta)$, where $\Delta\cos\theta = 0.2$. Figure 2 shows the typical $d\sigma/d\Omega$ distributions. The systematic uncertainty of $d\sigma/d\Omega$ is also given in Fig. 2. It includes the uncertainty of event selection in the kinematic fit, that of counting N_ω due to the $M_{\pi\gamma}$ threshold, that of acceptance owing to the uncertainties of the $d\sigma/d\Omega$ distributions for event generation in the simulation, that of detection efficiency of protons, and that of normalization resulting from N_τ and N_γ.

Every $d\sigma/d\Omega$ distribution shows a slight increase with increase of $\cos\theta$. A finite P-wave amplitude must produce asymmetric behavior of the angular distribution through the interference with the S-wave amplitude although the S-wave contribution is expected to be dominant near the threshold. The measured $d\sigma/d\Omega$s in this work are somewhat lower than the world available data. The obtained $d\sigma/d\Omega$ depends on the incident-energy coverage because the cross section increases rapidly as the incident energy goes up. The bin size of the incident energy is ≈4.5 MeV in our results, while 25 MeV for SAPHIR [10], 18 MeV for CLAS [11], and 15 MeV for A2 [4]. The event-weighted average of incident photon energies in a bin is higher than the median by 0.4–0.7, 3.4–4.2, 2.5–3.0, and 2.0–2.5 MeV for this work, SAPHIR, CLAS, and A2, respectively. In Fig. 2, the angular distribution obtained by the A2 collaboration at $E_\gamma \approx 1.14$ GeV shows a shape being concave upward, suggesting a P-wave contribution, although any significant slope changes are not observed in this work. Apparently this deviation comes from the relative difference of centroid photon-tagging energies by a few MeV. As shown in Fig. 3, the $d\sigma/d\Omega$ results in this work agree very well with those from other collaborations after increasing their incident photon energies by 10 MeV. Different steps of the incident energies among world available data allow us to take a discrete minimum shift of 10 MeV. The uncertainty of the centroid photon-tagging energies in this work is estimated to be 0.3%, which corresponds to 3.6 MeV. A calibration difference of photon-tagging energies needs to be incorporated in the estimation of the systematic uncertainty for $a_{\omega p}$ and $r_{\omega p}$.

The total cross section σ is obtained by integrating $d\sigma/d\Omega$s all over the ten emission-angle bins:

$$\sigma = \sum 2\pi\,\Delta\cos\theta\frac{d\sigma}{d\Omega}. \quad (3)$$

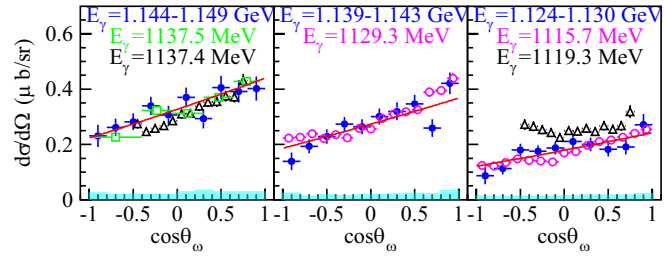

FIG. 3. Same as Fig. 2 but for different incident energies. The $d\sigma/d\Omega$ results from other collaborations are plotted by increasing their incident photon energies by 10 MeV.

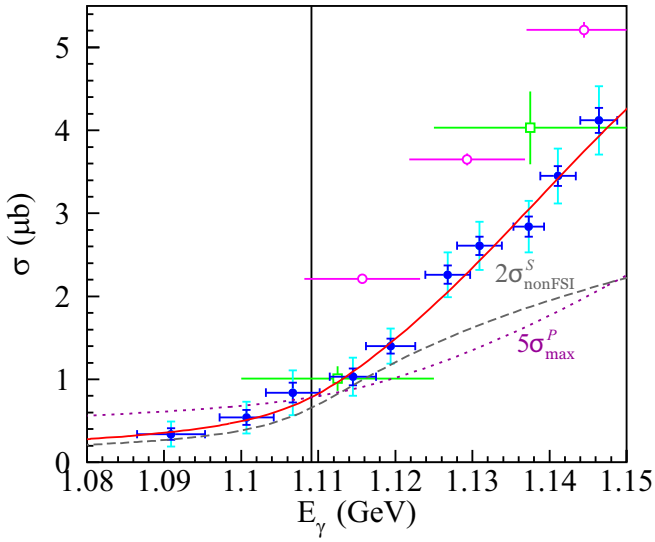

FIG. 4. Total cross section σ as a function of E_γ. The filled circles (blue) represent the measured σ in this work. Each horizontal bar indicates the incident-energy coverage. Each short vertical bar (blue) represents the statistical error of σ, and the connected bars (cyan) indicate the upper- and lower-side systematic error of σ. The vertical line (black) shows E_γ corresponding to the reaction threshold for production of ω having the centroid mass. The solid curve (red) shows the calculated excitation function with the parameters: $a_{\omega p} = -0.97 + i0.07$ fm and $r_{\omega p} = +2.78 - i0.01$ fm. The dashed curves (gray) show $2\sigma^S_{\rm nonFSI}$ where $\sigma^S_{\rm nonFSI}$ denotes the excitation function with $a_{\omega p} = 0$ fm and $r_{\omega p} = 0$ fm. The dotted curve (purple) shows $5\sigma^P_{\rm max}$ where $\sigma^P_{\rm max}$ stands for the upper limit of the P-wave contribution. The σ results from SAPHIR [10] and A2 [4] collaborations are depicted by open boxes (green) and open circles (magenta), respectively.

Figure 4 shows σ as a function of the incident photon energy. The excitation function shows a monotonic increase, and finite yields are observed below the threshold $E_\gamma^{\rm thr}$ for production of ω having the centroid mass. The obtained cross sections show a systematic deviation from the world available data but agree very well with them after increasing their incident photon energies by 10 MeV. Our results are plotted at the event-weighted average of the incident photon energies within a bin, while the results from other facilities are placed at the median of a bin. The data points should be placed at the 2.0–2.5 and 3.4–4.2 MeV higher energies for the A2 and SAPHIR data, respectively. The uncertainty of tagging-energy determination (0.3%) for the incident photon beam may account for the remaining deviation in part.

We determine $a_{\omega p}$ and $r_{\omega p}$ from the shape of the excitation function. We evaluate the excitation function for the $\gamma p \to \omega p$ reaction by using a model with final-state ωp interaction (FSI) based on the Lippmann-Schwinger equation. We assume that the S-wave contribution is dominant at $E_\gamma = 1.09$–1.15 GeV. The total cross section for a fixed ω mass M and γp-c.m. energy W can be calculated by using a transition amplitude $T_{\gamma p\to\omega p}(W, M)$:

$$\sigma_0(W, M) = \frac{1}{16\pi W^2}\frac{p(W, M)}{k}|T_{\gamma p\to\omega p}(W, M)|^2, \quad (4)$$

where k and p denote the momenta of initial- and a final-state particles, respectively, in the γp-c.m. frame. The total cross section σ as a function of E_γ is obtained by averaging $\sigma_0(W(E_\gamma), M)$ over available ω masses:

$$\sigma(E_\gamma) = \int_{m_{\pi^0}}^{W(E_\gamma)-m_p} \sigma_0(W(E_\gamma), M)L_\omega(M)dM, \quad (5)$$

where the probability $L_\omega(M)$ stands for a Breit-Wigner function with a centroid of $M_\omega = 782.65$ MeV and a width of $\Gamma_\omega = 8.49$ MeV [13].

The $T_{\gamma p\to\omega p}$ is expressed by

$$T_{\gamma p\to\omega p} = V_{\gamma p\to\omega p} + T_{\omega p\to\omega p}G_{\omega p\to\omega p}V_{\gamma p\to\omega p}, \quad (6)$$

where $T_{\omega p\to\omega p}$ stands for the ωp scattering amplitude, $G_{\omega p\to\omega p}$ denotes the ωp propagator, and $V_{\gamma p\to\omega p}$ is the production amplitude without FSI. We evaluate the matrix element for $T_{\gamma p\to\omega p}$ with on-shell approximations for $T_{\omega p\to\omega p}$ and $V_{\gamma p\to\omega p}$ and introduce a Gaussian form factor in the integration of $G_{\omega p\to\omega p}$. This leads the matrix element of $T_{\gamma p\to\omega p}$ to the equation:

$$\begin{aligned}\langle\omega p(p)|T_{\gamma p\to\omega p}|\gamma p(k)\rangle &= \langle\omega p(p)|V_{\gamma p\to\omega p}|\gamma p(k)\rangle + \int\langle\omega p(p)|T_{\omega p\to\omega p}|\omega p(q)\rangle\frac{\delta^3(\vec{q}-\vec{q}\,')}{W - H_0 + i\epsilon}\langle\omega p(q')|V_{\gamma p\to\omega p}|\gamma p(k)\rangle d\vec{q}d\vec{q}\,' \\ &\simeq \left[1 + 8\pi\mu\langle\omega p(p)|T_{\omega p\to\omega p}|\omega p(p)\rangle\int\frac{d\vec{q}}{p^2 - q^2 + i\mu\Gamma_\omega}\exp\left(-\frac{q^2}{\Lambda^2}\right)\right]\langle\omega p(p)|V_{\gamma p\to\omega p}|\gamma p(k)\rangle, \quad (7)\end{aligned}$$

where H_0 stands for the free Hamiltonian for the final-state ωp, and μ denotes a reduced mass between ω (with a mass of M) and the proton. Here, we use a cutoff parameter $\Lambda = 0.8$ GeV/c. $\langle\omega p(p)|T_{\omega p\to\omega p}|\omega p(p)\rangle$ is given by $a_{\omega p}$ and $r_{\omega p}$:

$$\langle\omega p(p)|T_{\omega p\to\omega p}|\omega p(p)\rangle = -\frac{1}{(2\pi)^2\mu}\left(\frac{1}{a_{\omega p}} + \frac{1}{2}r_{\omega p}p^2 - ip\right)^{-1}. \quad (8)$$

$\langle\omega p(p)|V_{\gamma p\to\omega p}|\gamma p(k)\rangle$ is assumed to be a constant value of one in the incident-energy region of interest.

The dashed curve (gray) in Fig. 4 shows the excitation function $\sigma^S_{\rm nonFSI}$ with $a_{\omega p} = 0$ fm and $r_{\omega p} = 0$ fm corresponding to non FSI condition, which does not reproduce the experimental data. FSI is necessary and the optimal set of $a_{\omega p}$ and $r_{\omega p}$ are determined to reproduce the experimentally obtained cross-section data. The χ^2 corresponding to the reproducibility is defined as

$$\chi^2 = \sum_{i=1}^{10}\frac{(\sigma_i - \alpha Y_i)^2}{\left(\delta\sigma_i^{(\rm stat)}\right)^2 + \left(\delta\sigma_i^{(\rm syst)}\right)^2}, \quad (9)$$

TABLE I. Deduced scattering parameters $a_{\omega p}$ and $r_{\omega p}$ for several conditions. The second, third, and fourth lines show the results for different Λ cutoff parameters. The fifth line corresponds to the result with taking the P-wave contribution into account where Im $r_{\omega p}$ is fixed at 0 fm. The sixth line represents the result with the assumption that the energy dependence of the ω production amplitude is expressed by a single N^* resonance as an extreme case.

Parameters	Re $a_{\omega p}$ (fm)	Im $a_{\omega p}$ (fm)	Re $r_{\omega p}$ (fm)	Im $r_{\omega p}$ (fm)
$\Lambda = 0.8$ GeV/c	$-0.97^{+0.16+0.03}_{-0.16-0.00}$	$+0.07^{+0.15+0.17}_{-0.14-0.09}$	$+2.78^{+0.67+0.11}_{-0.54-0.12}$	$-0.01^{+0.46+0.06}_{-0.50-0.00}$
$\Lambda = 0.6$ GeV/c	$-1.11^{+0.14+0.03}_{-0.16-0.04}$	$+0.12^{+0.17+0.12}_{-0.17-0.11}$	$+2.78^{+0.81+0.04}_{-0.57-0.16}$	$+0.00^{+0.44+0.11}_{-0.54-0.10}$
$\Lambda = 1.0$ GeV/c	$-0.89^{+0.16+0.01}_{-0.18-0.00}$	$+0.04^{+0.14+0.13}_{-0.12-0.04}$	$+2.78^{+0.62+0.23}_{-0.51-0.09}$	$+0.01^{+0.47+0.11}_{-0.50-0.05}$
P-wave contribution	$-0.96^{+0.16+0.04}_{-0.16-0.01}$	$+0.10^{+0.14+0.14}_{-0.14-0.09}$	$+2.85^{+0.77+0.15}_{-0.53-0.15}$	0.00
Single N^* contribution	$-0.87^{+0.15+0.04}_{-0.22-0.02}$	$+0.22^{+0.14+0.11}_{-0.12-0.11}$	$+2.69^{+0.62+0.06}_{-0.55-0.12}$	$-0.04^{+0.48+0.04}_{-0.69-0.14}$

where σ_i, $\delta\sigma_i^{(\mathrm{stat})}$, $\delta\sigma_i^{(\mathrm{syst})}$, and Y_i denote the measured total cross section, its statistical error, its systematic error, and the yield estimated in Eq. (5) by taking the coverage of incident energies into account, respectively, for the ith incident-energy bin. The coefficient α for the overall normalization is determined to minimize χ^2 for each parameter set. The deduced values are $a_{\omega p} = (-0.97^{+0.16+0.03}_{-0.16-0.00}) + i(0.07^{+0.15+0.17}_{-0.14-0.09})$ fm and $r_{\omega p} = (+2.78^{+0.67+0.11}_{-0.54-0.12}) + i(-0.01^{+0.46+0.06}_{-0.50-0.00})$ fm. The first and second errors for each parameter refer to the statistical and systematic uncertainties, respectively. The systematic uncertainty is estimated from that of the mean incident energy ($\pm 0.3\%$) for each photon-tagging bin. The solid (red) curve in Fig. 4 shows the excitation function with the optimal parameters. No significant changes are observed for the $a_{\omega p}$ and $r_{\omega p}$ parameters when we shift the incident photon energies by $\pm 0.3\%$.

The parameters may be somewhat affected by the adopted Λ. We also determine $a_{\omega p}$ and $r_{\omega p}$ for $\Lambda = 0.6$ and 1.0 GeV/c. The obtained values are summarized in Table I. Although $|\mathrm{Re}\, a_{\omega p}|$ and $|\mathrm{Im}\, a_{\omega p}|$ become larger with decreasing Λ, changes of $a_{\omega p}$ and $r_{\omega p}$ are not significant among the realistic Λ values.

The asymmetric behavior of the angular distribution mainly comes from interference between S- and P-wave contributions. The dotted curve (magenta) in Fig. 4 shows the shape of the P-wave excitation function where $\sigma_0^P(W, M) \propto p^3/k$ is assumed. The finite width of ω makes the P-wave excitation function rather flat, and the P-wave contribution does not explain the gap at higher incident energies between the data and calculation without FSI. We also fit the excitation function by adding a P-wave contribution to the experimental data by fixing Im $r_{\omega p} = 0$ fm, obtaining the values given in Table I. The optimal coefficient to the P-wave contribution is zero, and the P-wave total cross section is zero with an error of σ^P_{max}. The dotted curve in Fig. 4 corresponds to $5\sigma^P_{\mathrm{max}}$. The asymmetric behavior in the angular distribution shown in Figs. 2 and 3 requires a finite P-wave contribution. The solid curves in Figs. 2 and 3 correspond to a solution under the condition that the P-wave contribution in σ is $\sigma^P_{\mathrm{max}}/5$. We can conclude that the P-wave contribution in σ is negligibly small in the determination of $a_{\omega p}$ and $r_{\omega p}$.

We have assumed that $V_{\gamma p\to\omega p}$ is constant since the coverage of incident energies is narrow ($E_\gamma = 1.09$–1.15 GeV) for several overlapping N^* with a very wide width. We deduce the scattering parameters by assuming a single N^* contribution $D_{13}(1700)$ as an extreme condition:

$$V_{\gamma p\to\omega p} \propto (W^2 - M^2_{N^*} + iM_{N^*}\Gamma_{N^*})^{-1}, \tag{10}$$

where $M_{N^*} = 1.7$ GeV and $\Gamma_{N^*} = 0.2$ GeV [13]. The change of each parameter from the constant $V_{\gamma p\to\omega p}$ is not significant.

Figure 5 shows the real and imaginary parts of 1/2 and 3/2 spin-averaged $a_{\omega p}$ obtained by assuming a constant $V_{\gamma p\to\omega p}$ in this work together with the previously obtained values. It is consistent with $|a_{\omega p}| = 0.82 \pm 0.03$ fm given by the A2 Collaboration [4]. The other values correspond to the theoretical predictions. The positive Re $a_{\omega p}$ value is rejected at a confidence level higher than 99.9%. Taking into account the positive $r_{\omega p}$ value, the obtained $a_{\omega p}$ value gives repulsion, and no bound, resonance, or virtual state is expected [22]. The repulsion is found to be much stronger than the πN ones. Slightly attractive ω-nucleus (ωA) interactions are reported with potential depths at a normal nuclear density of $-42 \pm 17 \pm 20$ MeV [23] and $-15 \pm 35 \pm 20$ MeV [24] from ω photoproduction from nuclei. The measurement of the ω lineshape shows a decrease of ω mass by $9.2\% \pm 0.2\%$ (corresponding to ωA attraction) without any in-medium

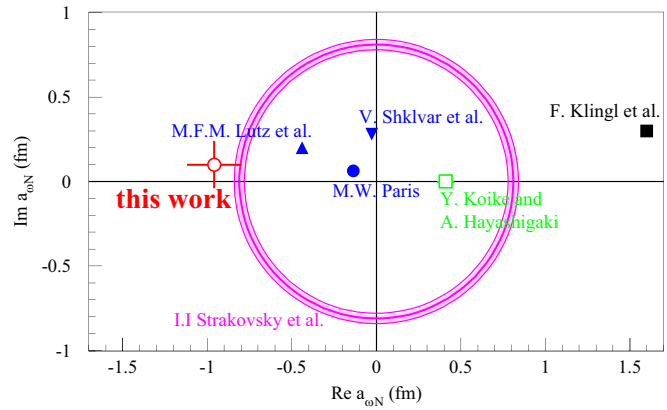

FIG. 5. Real and imaginary parts of spin-averaged $a_{\omega N}$ obtained in this work (red). The donut (magenta) represents the experimentally obtained $|a_{\omega N}|$ using a VMD model [4]. Other markers indicate $a_{\omega N}$s obtained in the theoretical works on an effective Lagrangian approach [5] (black), a QCD sum-rule analysis [6] (green), coupled-channel analyses [7–9] (blue).

broadening [25,26]. The relation between strong ωN repulsion and ωA attraction would be a subject of future discussions taking into consideration spin-dependent terms, higher partial waves, and partial restoration of chiral symmetry.

In summary, the total cross sections have been measured for the $\gamma p \to \omega p$ reaction near the threshold. The ω is identified through the $\omega \to \pi^0\gamma$ decay. The spin-averaged scattering length $a_{\omega p}$ and effective range $r_{\omega p}$ between the ω and proton are estimated from the excitation function at incident photon energies ranging from 1.09 to 1.15 GeV: $a_{\omega p} = (-0.97^{+0.16+0.03}_{-0.16-0.00}) + i(0.07^{+0.15+0.17}_{-0.14-0.09})$ fm and $r_{\omega p} = (+2.78^{+0.67+0.11}_{-0.54-0.12}) + i(-0.01^{+0.46+0.06}_{-0.50-0.00})$ fm. The real and imaginary parts for $a_{\omega p}$ and $r_{\omega p}$ are determined separately for the first time. A small P-wave contribution does not affect the obtained values. The positive Re $a_{\omega p}$ value indicates repulsion.

The authors express gratitude to the ELPH accelerator staff for stable operation of the accelerators in the FOREST experiments. They acknowledge Mr. Kazue Matsuda, Mr. Ken'ichi Nanbu, and Mr. Ikuro Nagasawa for their technical assistance in the FOREST experiments. They received help at the early stage of this work from Dr. Hiroyuki Kamano. They also thank Prof. Igor I. Strakovsky for providing all the available numerical values of cross sections for the $\gamma p \to \omega p$ reaction. They are grateful to Prof. Mark W. Paris for giving us the numerical values on the total cross sections of a single partial wave. One of the authors (T.I.) expresses heartfelt gratitude to Dr. Shuntaro Sakai for several useful conversations. This work was supported in part by the Ministry of Education, Culture, Sports, Science and Technology, Japan (MEXT) and Japan Society for the Promotion of Science (JSPS) through Grants-in-Aid for Specially Promoted Research Grant No. 19002003, for Scientific Research (A) Grants No. 24244022 and No. 16H02188, for Scientific Research (B) Grants No. 17340063 and No. 19H01902, for Scientific Research (C) Grant No. 26400287, and for Scientific Research on Innovative Areas Grants No. 18H05407 and No. 19H05141.

[1] R. Machleidt, Adv. Nucl. Phys. **19**, 189 (1989).
[2] H. Shen, H. Toki, K. Oyamatsu, and K. Sumiyoshi, Nucl. Phys. A **637**, 435 (1998).
[3] B. Abbott *et al.*, Phys. Rev. Lett. **119**, 161101 (2017).
[4] I. I. Strakovsky *et al.* (A2 Collaboration at MAMI), Phys. Rev. C **91**, 045207 (2015).
[5] F. Klingl, T. Waas, and W. Weise, Nucl. Phys. A **650**, 299 (1999).
[6] Y. Koike and A. Hayashigaki, Prog. Theor. Phys. **98**, 631 (1997).
[7] M. F. M. Lutz, Gy. Wolf, and B. Friman, Nucl. Phys. A **706**, 431 (2002); **765**, 495 (2006).
[8] V. Shklyar, H. Lenske, U. Mosel, and G. Penner, Phys. Rev. C **71**, 055206 (2005).
[9] M. W. Paris, Phys. Rev. C **79**, 025208 (2009).
[10] J. Barth *et al.* (SAPHIR Collaboration), Eur. Phys. J. A **18**, 117 (2003).
[11] M. Williams *et al.* (CLAS Collaboration), Phys. Rev. C **80**, 065208 (2009); M. Williams, *ibid.* **80**, 065209 (2009).
[12] A. Wilson *et al.* (CBELSA/TAPS Collaboration), Phys. Lett. B **749**, 407 (2015).
[13] M. Tanabashi *et al.* (Particle Data Group), Phys. Rev. D **98**, 030001 (2018).
[14] R. Hashimoto *et al.*, Few-Body Syst. **54**, 1135 (2013).
[15] T. Ishikawa *et al.*, JPS Conf. Proc. **10**, 031001 (2016).
[16] T. Ishikawa *et al.*, Nucl. Instrum. Methods Phys. Res., Sect. A **832**, 108 (2016).
[17] T. Ishikawa *et al.*, Nucl. Instrum. Methods Phys. Res., Sect. A **622**, 1 (2010); **811**, 124 (2016); Y. Matsumura *et al.*, *ibid.* **902**, 103 (2018); Y. Obara *et al.*, *ibid.* **922**, 108 (2019).
[18] F. Hinode *et al.*, in *Proceedings of 21st IEEE Particle Accelerator Conference (PAC)* (IEEE, Piscataway, 2005), pp. 2458–2460.
[19] T. Ishikawa *et al.*, Phys. Lett. B **772**, 398 (2017); **789**, 413 (2019).
[20] S. Agostinelli *et al.*, Nucl. Instrum. Methods Phys. Res., Sect. A **506**, 250 (2003); J. Allison *et al.*, IEEE Trans. Nucl. Sci. **53**, 270 (2006); GEANT4 website http://geant4.cern.ch/
[21] A. Fix and H. Arenhövel, Eur. Phys. J. A **25**, 115 (2005); 2-PION-MAID website https://maid.kph.uni-mainz.de/twopion/
[22] Y. Ikeda, T. Hyodo, D. Jido, H. Kamano, T. Sato, and K. Yazaki, Prog. Theor. Phys. **125**, 1205 (2011).
[23] V. Metag *et al.*, Prog. Part. Nucl. Phys. **67**, 530 (2012); V. Metag, Hyperfine Interact. **234**, 25 (2015).
[24] S. Friedrich *et al.* (CBELSA/TAPS Collaboration), Phys. Lett. B **736**, 26 (2014).
[25] K. Ozawa *et al.*, Phys. Rev. Lett. **86**, 5019 (2001).
[26] M. Naruki *et al.*, Phys. Rev. Lett. **96**, 092301 (2006).